THE JOURNAL OF PHYSICAL CHEMISTRY A

Article

Cite This: J. Phys. Chem. A 2019, 123, 2310−2319

pubs.acs.org/JPCA

Quantum Spin−Orbit Electronic State Selection of Atomic Transition Metal Vanadium Cation for Chemical Reactivity Studies

Published as part of The Journal of Physical Chemistry virtual special issue "Hai-Lung Dai Festschrift".

Yih Chung Chang, Bo Xiong, Yuntao Xu, and Cheuk-Yiu Ng*

Department of Chemistry, University of California, Davis, California 95616, United States

ABSTRACT: By combining a pulsed laser ablation vanadium atom (V) beam source with the two-color laser sequential electric field pulse scheme for pulse field ionization-photoion (PFI-PI) detection, we have developed a quantum spin−orbit state selected transition metal ion source for ion−molecule reaction studies. As a demonstration, we show that the V^+ ion can be prepared in the single spin−orbit levels of its three lowest quantum electronic states, $V^+[a^5D_J$ (J = 0−4), a^5F_J (J = 1−5), and a^3F_J (J = 2−4)], achieving laboratory kinetic energy (E_{lab}) resolutions of ≤0.2 eV. The precursor V atom beam is first excited to high-n Rydberg states by resonance-enhanced visible−ultraviolet laser photoexcitation via the $V^*[3d^3(^4F)4s4p\ (^3P^\circ)]$ neutral intermediate state. The total photon energy is tuned in the regions from 54 380 to 63 520 cm^{-1} to cover the photoionization energies for the formation of these spin−orbit states. Sharp Rydberg transitions converging to the $V^+[a^5D_J$ (J = 1 and 2)] spin−orbit levels are identified in the respective PFI-PI spectra for the $V^+[a^5D_J$ (J = 0 and 1)] states. The analysis of these Rydberg members observed yields an ionization energy of 54 412.65 ± 0.15 cm^{-1} for V atom, which is in excellent accord with the literature value of 54 413 ± 1 cm^{-1} eV. In order to understand the profile for the PFI-PI spectrum of V^+ ion observed and thus obtain reliable Stark shift corrections by using the sequential PFI-PI detection scheme, we have also examined the PFI-PI spectrum for $Ar^+(^2P_{3/2})$ in detail by varying the retarding as well as the PFI electric field pulses.

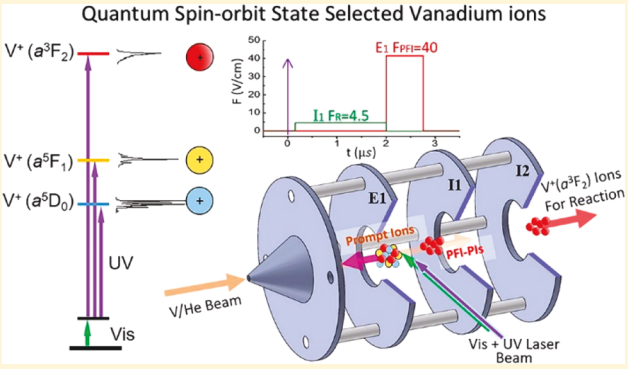

I. INTRODUCTION

Atomic transition metal cations play an important role in many research fields, particularly in organometallic ion chemistry and catalysis.[1−4] The ability of atomic transition metal cations to mediate the activation of selected chemical bonds is one of their distinct chemical characteristics, allowing the observation of specific chemical outcomes. Although practical catalytic processes occur mostly in condensed phases and interfaces, chemical dynamics and kinetics studies of atomic transition metal ion reactions in the gas phase have been shown to provide unambiguous chemical insight for idealized catalytic model systems without the influence of solvent and substrate effects.

Previously we have pointed out that chemical reactivity of ions can be determined precisely by absolute integral reaction cross section (σ) measurements of appropriate ion−molecule processes. Due to the ease of reactant and product ion mass identifications and the ability to control the center-of-mass collision energies (E_{cm}'s), σ measurements for a great number of ion−molecule reactions involving atomic transition metal cations have been performed as a function of E_{cm} using a variety of mass spectrometric techniques, including the guided ion beam and the Fourier transform ion cyclotron resonance mass spectrometry.[5,6] These mass spectrometric studies have provided a lion's share of our current understanding of organometallic ion chemistry in the gas phase. Since atomic transition metal cations are among the smallest transition metal entities exhibiting catalytic functions, the detailed study of the chemical reactivity of transition metal cations at the single atom level is valuable for gaining fundamental understanding of the bonding properties of transition metals.

According to the Born−Oppenheimer approximation, molecular geometry is predominantly determined by the electron arrangement; that is, the motions of the nuclei are governed by the potential energy surfaces set up by the electron distributions. Thus, we expect that the most effective means of promoting chemical reactivity is to alter the electron density distribution by quantum electronic state selection. Previous experimental and theoretical studies[3,7−9] have suggested that the existence of nearby manifolds of low-lying high-multiplicity electronic states plays a pivotal role in the distinctive bonding and reactivity properties of transition metal species. In order to unravel the complex ion chemistry present in atomic transition metal cations, such as the vanadium cation (V^+), it is necessary to perform quantitative measurements on chemical reactivity of the V^+ ion as a function of not only E_{cm}

Received: January 17, 2019
Revised: February 26, 2019
Published: February 28, 2019

DOI: 10.1021/acs.jpca.9b00511
J. Phys. Chem. A 2019, 123, 2310−2319

but also quantum spin−orbit electronic state. Furthermore, the electronic configuration of atomic transition metal cations depends on the spin−orbit coupling scheme. Hence, detailed reactivity measurements must involve the spin−orbit state selection of V^+ ion. However, due to the challenging preparation of spin−orbit and electronic states of the V^+ ion, electronic state selected chemical reactivity measurements of the V^+ ion performed as a function of spin−orbit and electronic state have not been achieved. This work reports the first success of single spin−orbit state preparations of the V^+ ion into its three lowest quantum electronic states, $V^+(a^5D_J)$, a^5F_J, and a^3F_J), which can then be used in ion−molecule reaction dynamics studies.

Table 1 lists the dominant electronic configurations of $3d^4$, $3d^3(^4F)4s$, and $3d^3(^4F)4s$ for the corresponding electronic states a^5D_J, a^5F_J, and a^3F_J of V^+ ion, along with the energies of their spin−orbit levels measured with respect to the a^5D_0 ground electronic state, which is arbitrarily set to 0 cm^{-1}.[10] The spin−orbit averaged energies for the first and second excited electronic states, a^5F_J and a^3F_J, respectively, are higher than that of the ground a^5D_J electronic state of V^+ ion by 0.3 and 1.1 eV, respectively. These relatively small electronic energy gaps between the low-lying electronic states result from the near degeneracy of the 4s and 3d orbitals of V^+ ion. Although the a^5F_J and a^3F_J states have the same electronic configuration, the total spins of electrons are different. The higher energy of the low spin state a^3F_J compared to the high spin state a^5F_J can be attributed to the electron pairing energy. Invoking spin−orbit interactions, these three lowest electronic states $V^+[a^5D_J$ (J = 0−4), a^5F_J (J = 1−5), and $a^3F_J(J$ = 2−4)] consist of a total of 13 spin−orbit levels. Furthermore, since the main electronic configurations for these low-lying electronic states of V^+ essentially involve only 4s and 3d atomic orbitals, optical transitions between these electronic states are parity forbidden, resulting in long radiative lifetimes for these electronic states, which are expected to be significantly longer than the present experimental measurement cycle of ≈100 μs.[11−13]

Table 1. Electronic Configurations, Term Symbols, and Spin−Orbit or J Level Energies in cm^{-1} of the Three Lowest Electronic States of Vanadium Cation[10]

electronic configuration	term symbol	J	J level energy[a] (cm^{-1})
$3d^4$	a^5D	0	0.0000 ± 0.0030
		1	36.1017 ± 0.0012
		2	106.6421 ± 0.0010
		3	208.7901 ± 0.0008
		4	339.1256 ± 0.0013
$3d^3(^4F)4s$	a^5F	1	2605.0400 ± 0.0012
		2	2687.2090 ± 0.0090
		3	2808.9590 ± 0.0008
		4	2968.3883 ± 0.0010
		5	3162.9673 ± 0.0023
$3d^3(^4F)4s$	a^3F	2	8640.3641 ± 0.0010
		3	8842.0507 ± 0.0006
		4	9097.8891 ± 0.0008

[a]The spin−orbit or J level energies are measured with respect to the a^5D_J (J = 0) ground state, which is arbitrarily set at zero. From ref 10, NIST Atomic Spectra Database (version 5.6.1).

The ion−molecule reactions between V^+ ions and simple neutral molecules have been considered as model reaction systems for fundamental investigation of the chemical reactivity of atomic transition metal cations. Early σ measurements have placed great emphasis on the importance of quantum state selections of V^+ ion. A variety of ion sources were used to produce V^+ ions in previous studies, including the surface ionization,[14,15] electron impact,[15,16] discharge flow tube,[16] resonance enhanced laser photoionization,[17,18] and laser ablation[19] sources. Most of these ion sources were found to be suitable for the preparation of V^+ ions predominantly in the a^5D_J ground electronic state or in a mixture of the ground and excited electronic states. Furthermore, these ion sources lacked the energy resolution to resolve individual spin−orbit states of the V^+ ion, and thus, spin−orbit state selected σ measurements were out of reach using these ion sources. Previous ion−molecule reaction studies reported that by changing the filament temperature in a surface ionization ion source or the electron energy of an electron impact ion source, the electronic state population of V^+ ions was found to be altered[15] as manifested by higher reaction cross sections observed for the V^+ reaction occurring in excited electronic states. However, the fact that the energy separation between the ground a^5D_J state and the second excited a^3F_J state is more than 1.1 eV makes it impractical to prepare excited $V^+(a^3F_J)$ ions by thermal Boltzmann excitation. Furthermore, due to the difficulty in identifying the first excited $V^+(a^5F_J)$ electronic state, which is 0.3 eV above the ground a^5D_J electronic state, no chemical reactivity or σ measurements have been reported for the $V^+(a^5F_J$ and $a^3F_J)$ states. Upon the basis of the above discussion, we may conclude that σ measurements reported previously are more reliable for the $V^+(a^5D_J)$ ground state, whereas accurate σ measurements for the excited $V^+(a^5F_J$ and $a^3F_J)$ electronic states remain to be investigated.

A one-color resonance-enhanced two-photon laser photoionization ion source has also been used in previous chemical reactivity studies of V^+ cation, where photoelectron time-of-flight (TOF) spectra are simultaneously recorded with photoionization measurements, the analysis of which is expected to yield the distribution of internal state populations.[18] However, the photoelectron TOF measurements lack the energy resolution to resolve some spin−orbit states involved. We note that photoions formed by one-color resonance-enhanced multiphoton ionization, which usually involve the use of a focused laser beam, could have complication in ion state assignments due to the possibility of absorbing additional laser photons.

In the past few years, we have developed a robust single-photon vacuum ultraviolet (VUV) laser sequential electric field pulse PFI-PI ion source that can readily be used to prepare small molecular ions in selected rovibronic states with essentially 100% purity for ion−molecule collision studies. These quantum state selected ions include $N_2^+(X^2\Sigma_g^+$: v^+ = 0−2; N^+ = 0−9),[20−24] $H_2O^+(X^2B_1$, $\nu_1^+\nu_2^+\nu_3^+$ = 000, 020, 100; N^+_{Ka+Kc+} = 0_{00}−3_{22}),[25−28] $H_2^+(X^2\Sigma_g^+$, v^+ = 1−3; N^+ = 0−3),[29] $O_2^+(a^4\Pi_{u5/2,3/2,1/2,-1/2}$, v^+ = 1−2; J^+),[30] and $O_2^+(X^2\Pi_{g3/2,1/2}$, v^+ = 22−23; J^+).[30] Encouraged by the success of the single-photon VUV laser PFI-PI scheme for quantum state selection of these main group molecular ions, we have further developed the two-color visible−ultraviolet (VIS−UV) laser PFI-PI scheme for quantum state selections of atomic transition metal V^+ cation. This article reports on the detailed procedures for using this VIS−UV laser PFI-PI scheme to prepare V^+ ion

DOI: 10.1021/acs.jpca.9b00511
J. Phys. Chem. A 2019, 123, 2310−2319

in single spin−orbit electronic states for fundamental chemical dynamics studies.

In order to learn about the PFI-PI mechanism and thus deduce reliable Stark shift corrections by simulations of the profiles for the PFI-PI spectra observed by using the sequential electric field pulse scheme, we have also performed a detailed PFI-PI measurement of $Ar^+(^2P_{3/2})$ ion by varying the retarding electric field pulse (F_R) as well as the PFI electric field pulse (F_{PFI}) applied to the ion source as described below.

II. EXPERIMENTAL CONSIDERATIONS

The experimental arrangement and procedures used in the present two-color VIS−UV laser PFI-PI study of V^+ cation are similar to previous single-photon VUV laser PFI-PI studies except that the VUV laser source is replaced by the two-color VIS−UV laser source. This experiment used part of the PFI-PI double-quadrupole−double-octopole (DQDO) ion−molecule apparatus, particularly the microchannel plate (MCP) ion detector located at the dc quadrupole ion bender, and the Daly type ion detector situated at the back of the product quadrupole mass filter, which has also been described in detail previously.[21] Here, we aim to focus on the implementation of the two-color VIS−UV laser PFI-PI ion source to the DQDO apparatus and its application to prepare V^+ ions in selected spin−orbit levels of the three lowest electronic states, $V^+[a^5D_J$ (J = 0−4)], $V^+[a^5F_J$ (J = 1−5)], and $V^+[a^3F_J$ (J = 2−4)], for chemical reaction dynamics studies.

(a) Two-Color Visible−UV Laser Excitation Scheme. Figure 1 depicts the schematic diagram for the two-color VIS-UV laser resonance-enhanced excitation scheme employed in this work. Two tunable dye lasers pumped by one identical Nd:YAG laser operated at 30 Hz were used as the excitation (ω_1) and ionization (ω_2) lasers for measurements of the PFI-PI spectra for $V^+[a^5D_J$ (J = 0−4)], $V^+[a^5F_J$ (J = 1−5)], and $V^+[a^3F_J$ (J = 2−4)]. The first dye laser was pumped by the third harmonic output (355 nm) of the Nd:YAG laser and was fixed at ω_1 = 21 841.4 cm^{-1} (or 457.845 nm). As shown in the figure, this VIS ω_1 output matches the transition of V atom from the neutral $V(3d^34s^2, a^4F_{3/2})$ ground state to the neutral $V^*[3d^3(^4F)\ 4s4p\ (^3P°), z^4G°_{5/2}]$ intermediate state.[10] The second dye laser was pumped by the second harmonic output (532 nm) of the same Nd:YAG laser to obtain fundamental output in wavelength range of 607.6−614.6 nm, which was then frequency doubled by a BBO crystal along with a beam path compensator to generate the UV ω_2 output range of 308.276−303.780 nm (32 438.5−32 918.6 cm^{-1}) for the preparation of the $V^+[a^5D_J$ (J = 0−4)] PFI-PIs. The VIS ω_1 and UV ω_2 beams were merged by using a dichroic mirror with the UV ω_2 laser beam pulse delayed by 10 ns with respect to the VIS ω_1 laser beam pulse. This two-color VIS−UV laser excitation of V atom results in the formation of excited V atoms in high-n Rydberg states [$V^*(n)$] converging to different spin−orbit levels of the ground electronic state $V^+(a^5D_J)$. Thus, the sum ($\omega_1 + \omega_2$) gives the total excitation laser photon energy range of 54 380−54 760 cm^{-1}, needed to cover the formation of $V^+[a^5D_J$ (J = 0−4)] PFI-PIs. The same experimental procedures are used for the formation of $V^+[a^5F_J$ (J = 1−5) and $V^+[a^3F_J$ (J = 2−4)] PFI-PIs except that the tunable UV ω_2 ranges used are 35 128.6−35 758.6 and 41 178.6−47 678.6 cm^{-1}, which correspond to the ($\omega_1 + \omega_2$) ranges of 56 970−57 600 and 63 020−63 520 cm^{-1}, respectively.

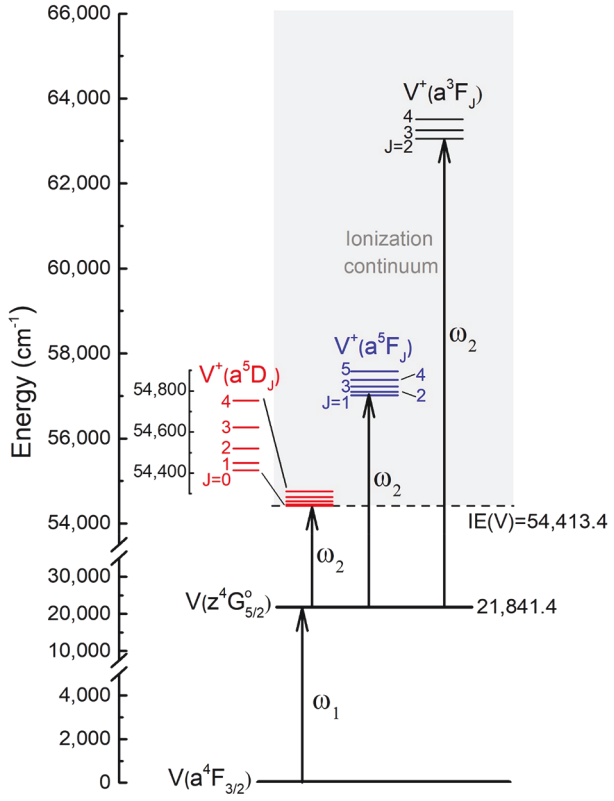

Figure 1. Schematic diagram for the two-color VIS−UV laser resonance-enhanced excitation scheme. The visible dye laser was fixed at ω_1 = 21 841.4 cm^{-1} to excite V atom from the neutral $V(3d^34s^2, a^4F_{3/2})$ ground state to the neutral $V^*[3d^3(^4F)\ 4s4p(^3P°), z^4G°_{5/2}]$ intermediate state, and the ultraviolet dye laser (ω_2) was tuned to perform measurements of the PFI-PI spectra for $V^+[a^5D_J$ (J = 0−4)], $V^+[a^5F_J$ (J = 1−5)], and $V^+[a^3F_J$ (J = 2−4)].

A modified Smalley-type[31] laser ablation metal beam source was used to produce precursor V atom sample in the form of a pulsed supersonically cooled gas jet. The detailed experimental arrangement and procedures for using this laser ablation metal atom beam source have been described previously.[32,33] The second harmonic output (532 nm, pulse energy = 2 mJ) of a Nd:YAG laser operated at 30 Hz was used to ablate a rotating V rod (99% purity). The V gas plumes thus produced were merged into the pulsed He-gas flow generated by a pulsed valve operated at 30 Hz and a He stagnation pressure of 40 psi. The cooling of the V gas plumes occurred in the capillary by collisions with the He carrier gas as well as by the supersonic expansion as the mixed V/He gas exited the capillary. The generation of the V gas plume and the introduction of the He gas flow were synchronized to achieve the optimal cooling of the V/He beam. In order to introduce a supersonic V atom beam into the photoexcitation (PEX) center with low divergence, two conical skimmers (diameter = 2 and 3 mm) were used at 10−12 cm downstream from the beam source to shape the V atom beam before entering the PEX region of the DQDO ion−molecule reaction apparatus.

(b) Sequential Electric Field Pulse Schemes for State-Selected PFI-PI Production. At the PEX center, the V atom beam intersects the VIS ω_1 and UV ω_2 laser beams perpendicularly, resulting in the excitation of V atoms in high-n Rydberg states [$V^*(n)$]. The subsequent application of the sequential electric field pulse scheme for retarding of

DOI: 10.1021/acs.jpca.9b00511
J. Phys. Chem. A 2019, 123, 2310−2319

prompt ions and PFI of V*(n) in PFI-PI measurements follows the same procedures as described previously.[21] Briefly, the ion source consists of three essential ion lenses, E1, I1, and I2, where the spacing between lenses E1 and I1 is defined as the PEX region. Lens I2, situated next to I1, can be used to block out prompt ions from exiting the ion source. The operation of the sequential electric field pulse scheme depends on the application of two electric field pulses F_R and F_{PFI} in V/cm at the PEX region as well as the potential energy barrier applied to lens I2. The time cycle for the application of the sequential electric field pulses on lenses E1, I1, and I2 is shown in the inset of Figure 2, in which the amplitude of the electric field

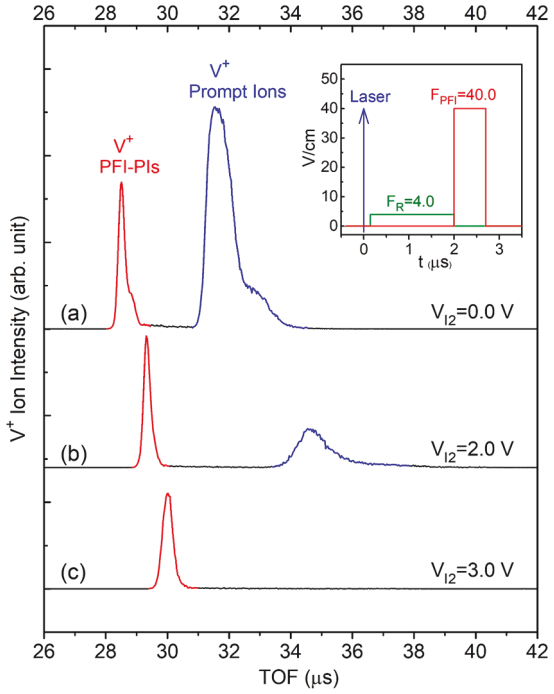

Figure 2. Comparison of the TOF spectra for V^+ PFI-PIs (red) and prompt ions (blue) obtained by using different dc voltage values (V_{I2}) of (a) 0.0, (b) 2.0, and (c) 3.0 V at lens I2. In these PFI-PI measurements, the same sequential electric field pulses F_R (amplitude = 4.0 V/cm, duration = 2 μs) and F_{PFI} (amplitude = 40 V/cm, duration = 0.7 μs) were applied to lenses E1 and I1, respectively. The timing sequence for applying the sequential electric field pulse scheme to lenses E1 and I1 for PFI-PI detection is shown in the inset.

pulse applied to the PEX region is plotted as a function of time. Here, time zero is taken to be the time when the VIS−UV lasers are turned on to intersect the V atom beam in the PEX center. During the laser excitation, the PEX region was maintained field free. After a delay of 150 ns with respect to the laser excitation, F_R was applied at lens I1 for 2 μs to retard prompt ions, resulting in the spatially separation of the prompt ions from the PFI-PIs as shown by the TOF spectra for the PFI-PIs and prompt ions in Figure 2a. Immediately after the switch-off of the F_R pulse, the F_{PFI} pulse is applied to ion lens E1 for 0.7 μs, serving to Stark field ionize the V*(n) species to generate PFI-PIs as well as to extract ions out of the PEX region. We have previously pointed out that to avoid the kinetic energy spread of PFI-PIs, it is necessary to use a sufficiently narrow F_{PFI} pulse, such that the F_{PFI} is switched off before the PFI-PIs exit the PEX region. In such a case, all PFI-PIs gain the same linear momentum, and thus, the kinetic energy resolution of the V^+ PFI-PI beam should approach that of the neutral V/He supersonic beam.

Figure 2a, Figure 2b, and Figure 2c compare the TOF spectra for V^+ PFI-PIs and prompt ions obtained by using different dc potential energy barrier values of 0.0, 2.0, and 3.0 V at lens I2, where the same sequential electric field pulses F_R (amplitude = 4.0 V/cm, duration = 2 μs) and F_{PFI} (amplitude = 40 V/cm, duration = 0.7 μs) were applied to lenses E1 and I1, respectively. These TOF spectra were measured by using the dual MCP ion detector located at the DC quadrupole ion bender. When lens I2 is set at 0.0 V, the potential barrier is zero, and thus both V^+ PFI-PIs and prompt ions passed through lens I2 and were detected as shown by upper TOF spectrum of Figure 2a. As expected, the V^+ PFI-PIs, which possess higher kinetic energies, arrived at the ion detector earlier than the prompts ions, and the V^+ PFI-PIs are well-separated from the prompt ions despite that the intensity of the prompt ions is significantly greater than that of the PFI-PIs. The TOF spectrum depicted in Figure 2b was measured by applying a dc voltage of 2.0 V at lens I2, resulting in a significant decrease in intensity for the prompt ions, whereas the intensity for V^+ PFI-PIs remains nearly the same compared to that of Figure 2a. This observation indicates that a large fraction of prompt ions was blocked out using a blocking voltage of 2.0 V. As shown in Figure 2c, we find that a dc voltage of 3.0 V applied to lens I2 was sufficient to completely block out prompt ions from exiting the PEX region, and thus, only quantum spin−orbit state selected V^+ PFI-PIs exited the PEX region and were guided to enter the radiofrequency (rf)-octopole reaction gas cell, where ion−molecule reaction with a neutral reactant occurs.

Blocking the prompt ions by setting a potential barrier at lens I2 as described above represents one practical method to prepare a pure beam of spin−orbit state selected V^+ PFI-PIs. We show in Figure 3a, Figure 3b, and Figure 3c the TOF spectra for the V^+ PFI-PIs and prompt ions observed by applying different F_R values of 0.0, 2.0, and 4.5 in V/cm at lens I1, where the F_{PFI} set at E1 was kept at 41.7 (V/cm). Here, the TOF spectra of Figure 3a−c were recorded by using the rear Daly type ion detector of the DQDO apparatus,[21] and thus the ion flight time range is longer than that shown in Figure 2a−c. For F_R = 0.0 V/cm, the TOF spectrum of Figure 3a, as expected, appeared as a single broad peak, indicating V^+ PFI-PIs and prompt ions exited from the ion source at the same time range. As the F_R was raised to 2.0 V/cm, the prompt ion peak was found to near complete separation from the V^+ PFI-PI peak as shown in the TOF spectrum of Figure 3b. The fact that the TOF spectrum of Figure 3c observed at F_R = 4.5 V/cm exhibits only the V^+ PFI-PI peak indicates that the prompt ions have exited and escaped the PEX region through lens E1 (in a direction opposed to the V^+ PFI-PI beam direction). That is, this mode of operation involving the use of a higher F_R value, but does not involve lens I2, can be a practical alternative for eliminating the prompt ions.

(c) Laboratory Kinetic Energy Measurements. In previous PFI-PI measurements based upon the application of the sequential electric field pulse scheme, narrow laboratory kinetic energy spreads (ΔE_{lab}'s) are observed down to 30−50 meV.[21] As described previously, the E_{lab} for V^+ can be determined by the retarding potential energy curve method using the rf-octopole reaction gas cell. Figure 4 shows a typical retarding potential energy curve for $V^+(a^3F_J)$ ions prepared in the present study; the analysis of retarding curve yields an E_{lab}

DOI: 10.1021/acs.jpca.9b00511
J. Phys. Chem. A 2019, 123, 2310−2319

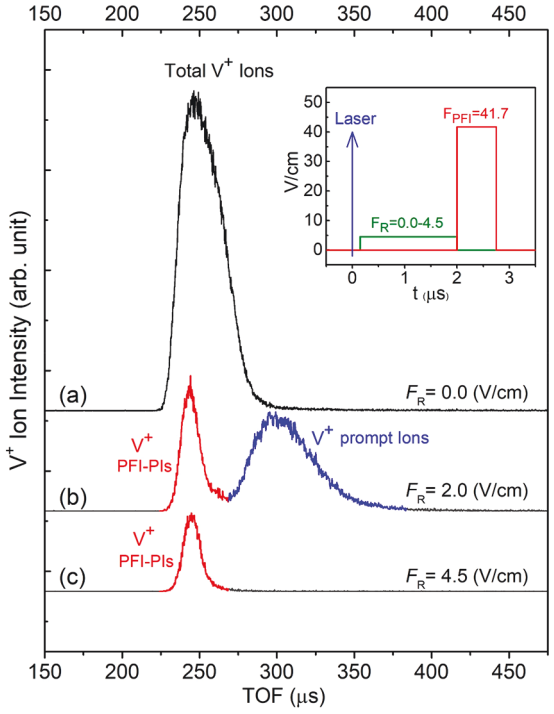

Figure 3. TOF spectra for the V^+ PFI-PIs (red) and prompt ions (blue) observed by using different F_R amplitudes of (a) 0.0, (b) 2.0, and (c) 4.5 V/cm, where the F_{PFI} set at E1 was kept the same as 41.7 V/cm. For F_R = 0.0 V/cm, the TOF spectrum (top curve) appeared as a single broad peak. For F_R = 2.0 V/cm, the TOF spectrum of (b) shows that the prompt ion peak is near complete separation from the V^+ PFI-PI peak. The TOF spectrum of (c) observed at F_R = 4.5 V/cm (bottom curve) exhibits only the V^+ PFI-PI peak, indicating that the prompt ions exited the PEX region through lens E1 prior to the application of F_{PFI}. The timing sequence for applying the sequential electric field pulse scheme to lenses E1, I1 for PFI-PI detection is shown in the inset.

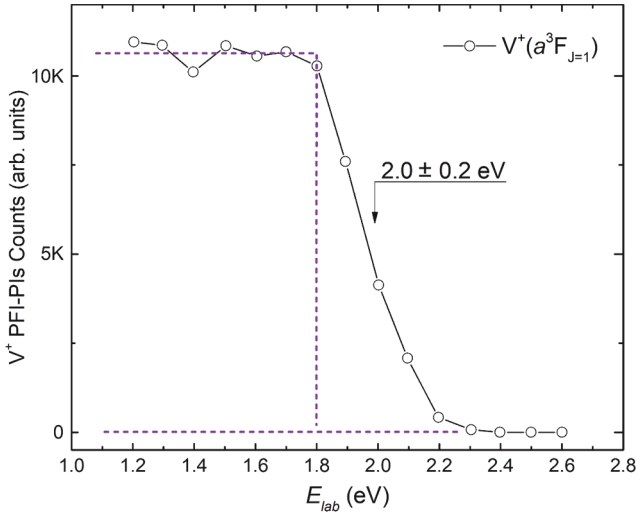

Figure 4. Retarding potential energy curve for $V^+(a^3F_1)$ ion. The analysis of this retarding curve gives E_{lab} = 2.0 ± 0.2 eV for the laboratory kinetic energy of V^+ PFI-PIs ion.

value of 2.0 ± 0.2 eV. Since the ion beam formation in this experiment involves the generation of plasma plumes, the relatively larger error limit of $\Delta E_{lab} \approx \pm 0.2$ eV (fwhm) determined here compared to previous PFI-PI measurements may be caused partially by the space charge effect.

III. RESULTS AND DISCUSSION

In the present VIS−UV laser PFI-PI experiment, the profile of the PFI-PI peak observed is expected to depend on both the retarding electric field pulse F_R and the PFI electric field pulse F_{PFI}. It is well-known that the presence of a pulsed electric field F in V/cm can induce a Stark shift $\Delta E = a(\sqrt{F})$ in cm^{-1}, where the coefficient a is known to depend on the detailed PFI scheme used, and ΔE is the decrease in ionization energy (IE) in cm^{-1}. Previous Stark shift studies using a pulsed field have yielded a values in the range of 3.8−4.1.[34,35]

(a) VUV Laser PFI-PI Spectra for $Ar^+(^2P_{3/2})$. In order to perform a proper analysis and thus obtain a reliable energy calibration for the present PFI-PI measurements based on the sequential electric field pulse scheme, we have performed a detailed Stark shift study on the VUV laser PFI-PI detection of $Ar^+(^2P_{3/2})$. This PFI-PI study for $Ar^+(^2P_{3/2})$ is aimed to reveal the F_R and F_{PFI} effects on the Stark shift. $Ar/Ar^+(^2P_{3/2})$ was selected as an energy calibration system because the IE(Ar) is known to a very high precision.[36]

The PFI-PI spectra for $Ar^+(^2P_{3/2})$ obtained by VUV laser PFI-PI measurements based on the sequential electric field pulse scheme using different combinations of F_R and F_{PFI} values are shown in Figure 5a and Figure 5b. Individual PFI-PI spectra shown in Figure 5a and Figure 5b were obtained by averaging at least three independent repeatable scans. For the five spectra shown from top to bottom in Figure 5a, all F_{PFI} values were kept at 6.3 V/cm, while the F_R values were set correspondingly at 1.0, 1.5, 2.0, 3.0, and 4.0 V/cm. The PFI-PI spectra for $Ar^+(^2P_{3/2})$ thus obtained have been simulated by Gaussian peak profiles using the Peak Fit software.[37] These PFI-PI spectra are found to be composed of two Gaussian components. The major one is originated from the cold supersonic Ar beam, and the weak one can be attributed to the thermal Ar gas in the experimental chamber. The central peak positions of the major Gaussian components obtained by Gaussian simulations are marked by short drop lines in the PFI-PI spectra of Figure 5a. As shown in this figure, the $Ar^+(^2P_{3/2})$ PFI-PI peak shifts toward lower energy as F_R is increased.

The top four $Ar^+(^2P_{3/2})$ PFI-PI spectra depicted in Figure 5b were obtained with F_R held at 4.0 V/cm while changing F_{PFI} as 6.3, 7.9, 9.5, and 11.0 V/cm. The bottom $Ar^+(^2P_{3/2})$ PFI-PI spectrum was obtained with F_R and F_{PFI} held at 3.6 and 19.5 (V/cm), respectively. For both Figure 5a and Figure 5b, the IE(Ar) position was marked by a vertical arrow. Under these PFI conditions, the high energy edges (marked in the figures by the dashed line) of all these $Ar^+(^2P_{3/2})$ PFI-PI spectra are found to shift to lower energies by the ΔE amount as predicted by the Stark shift formula $\Delta E = a(\sqrt{F_R})$ for F_R = 4.0 or 3.6 V/cm. The near complete depletion of the PFI-PI signal in this ΔE region up to the IE(Ar) can be attributed to Stark field ionization and the subsequent rejection of these PFI-PIs by using the sequential electric field pulse scheme as described above. As F_{PFI} is increased from 6.3 to 19.5 (V/cm), the PFI-PI peak position was found to shift lower still and have a larger width. The $Ar^+(^2P_{3/2})$ PFI-PI spectra shown in Figure 5a and Figure 5b reveal that both the F_R and F_{PFI} pulses affect the profile of the PFI-PI spectrum and contribute to the Stark shift.

(b) PFI-PI Mechanism for the Sequential Electric Field Pulse Scheme. The $Ar^+(^2P_{3/2})$ PFI-PI measurements are

DOI: 10.1021/acs.jpca.9b00511
J. Phys. Chem. A 2019, 123, 2310−2319

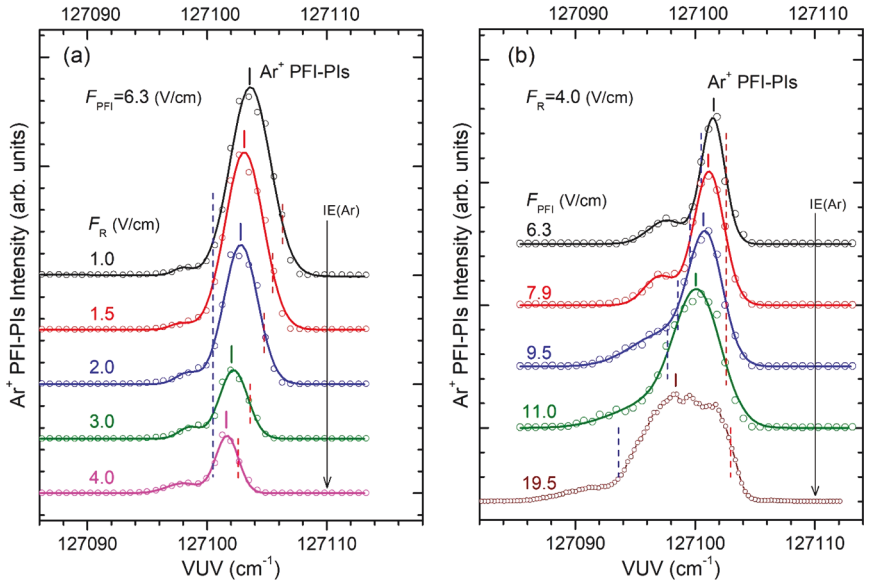

Figure 5. PFI-PI spectra for $Ar^+(^2P_{3/2})$ obtained by VUV laser PFI-PI measurements based on the sequential electric field pulse scheme using different combinations of F_R and F_{PFI} amplitudes. (a) For the five spectra shown from top to bottom, all F_{PFI} values were kept at 6.3 V/cm while the F_R values were set correspondingly at 1.0, 1.5, 2.0, 3.0, and 4.0 V/cm. (b) The four $Ar^+(^2P_{3/2})$ PFI-PI spectra shown from top to forth were obtained with F_R held at 4.0 V/cm with F_{PFI} set at 6.3, 7.9, 9.5, and 11.0 V/cm. The bottom $Ar^+(^2P_{3/2})$ PFI-PI spectrum was obtained with F_R held at 3.6 V/cm and F_{PFI} set at 19.5 V/cm. Under these PFI conditions, the high energy ends (marked by dotted lines) of all these $Ar^+(^2P_{3/2})$ PFI-PI spectra are found to shift to lower energies by the Stark shift of $\Delta E = a(\sqrt{F_R})$ as marked by vertical dotted lines in the spectra. The low energy ends of all $Ar^+(^2P_{3/2})$ PFI-PI spectra are shifted by $\Delta E = a(\sqrt{F_{PFI}})$, which are also marked by dotted lines in the spectra. Here the a-coefficient used is 3.72 obtained by the linear least-squares fits shown in Figure 7 (see the text).

found to be consistent with the Stark shift mechanism described below. A schematic diagram illustrating the mechanism for PFI-PI production using the sequential electric field pulse scheme is given in Figure 6. Since Stark shift ΔE depends on the amplitudes of F_R and F_{PFI} and that $F_R < F_{PFI}$, F_R and F_{PFI} are used to define PFI zone 1 and zone 2, respectively. Zone 1 covers the energy range between the IE and IE $- a(\sqrt{F_R})$. As pointed out above, for high-n Rydberg species populated by laser excitation in zone 1, they were ionized and dispersed and thus were not detected. The high-n Rydberg species populated in zone 2 (covers the energy region between IE $- a(\sqrt{F_R})$ and IE $- a(\sqrt{F_{PFI}})$) were ionized and detected as PFI-PIs. Thus, the PFI-PI spectrum for each spin–orbit state is expected to be confined in zone 2 in the present study.

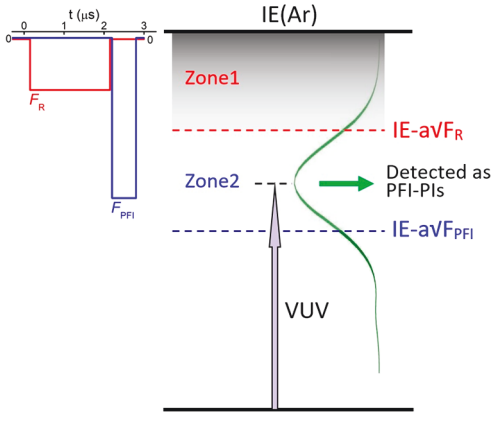

Figure 6. Schematic diagram illustrating the mechanism for PFI-PI production in using the sequential electric field pulse scheme. Since Stark shift ΔE depends on the amplitudes of F_R and F_{PFI}, F_R and F_{PFI} can be used to define PFI zone 1 and zone 2, respectively. Zone 1 covers the energy range between the IE and IE $- a(\sqrt{F_R})$. The high-n Rydberg species populated in zone 2 covers the energy region between IE $- a(\sqrt{F_R})$ and IE $- a(\sqrt{F_{PFI}})$. Thus, the PFI-PI spectrum is expected to be confined in zone 2.

Assuming that the maximum PFI-PI intensity, i.e., the central PFI-PI peak position, is observed at the middle photoexcitation energy of zone 2, the Stark shift for the PFI-PI peak ΔE can be calculated as $\Delta E = (a/2)[\sqrt{F_R} + \sqrt{F_{PFI}}]$, and the photoexcitation energy (E) at the PFI-PI peak position is related to the IE and the F_R and F_{PFI} amplitude values according to eq 1.

$$E = \mathrm{IE} - \Delta E = \mathrm{IE} - (a/2)[\sqrt{F_R} + \sqrt{F_{PFI}}] \quad (1)$$

On the basis of the Gaussian profile simulations, the central photoexcitation peak energies of the $Ar^+(^2P_{3/2})$ PFI-PI spectra shown in Figure 5a and Figure 5b are determined as E = 127 103.55, 127 103.1, 127 102.8, 127 102.05, 127 101.6, 127 101.1, 127 100.7, and 127 098.38 (cm^{-1}). For the bottom $Ar^+(^2P_{3/2})$ PFI-PI spectrum depicted in Figure 5b, it cannot be simulated by using the Gaussian profile fit. In this case, the peak energy at 127 098.38 cm^{-1} was adopted as the photoexcitation peak energy. These nine E values have been least-squares-fitted to a linear function of $(^1/_2)[\sqrt{F_R} + \sqrt{F_{PFI}}]$ according to eq 2 as shown in Figure 7 to determine the Stark shift a coefficient and the IE(Ar) by the respective slope and intercept. These least-squares fits yield a = 3.72 ± 0.07 and IE(Ar) = 127 110.03 ± 0.15 (cm^{-1}), which are found to be in excellent agreement with the literature values of 3.89 [34] and 127 109.825 ± 0.015 [36] (cm^{-1}), respectively. The error limits observed in the present study are consistent with the optical bandwidth of 0.15 cm^{-1} (fwhm) of the VUV laser used.

We note that eq 1 is based on the assumption that the central PFI-PI peak position can be located by a Gaussian

DOI: 10.1021/acs.jpca.9b00511
J. Phys. Chem. A 2019, 123, 2310–2319

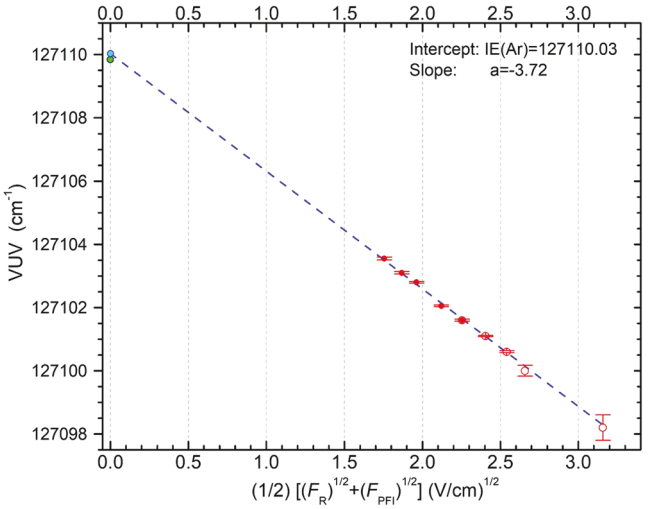

Figure 7. Measured E values (solid and open red circles) were least-squares-fitted (blue dash line) to a linear function of $(^1/_2)[\sqrt{F_R} + \sqrt{F_{PFI}}]$ according to eq 1 to determine the Stark shift a coefficient and the IE(Ar) by the respective slope and intercept. The least-squares fits yield a = 3.72 ± 0.06 and IE(Ar) = 127 110.03 ± 0.15 cm^{-1} (blue solid circle). The precise IE(Ar) = 127 099.825 ± 0.015 cm^{-1} reported by the previous work[36] was depicted as solid green circle.

instrumental profile fit of the PFI-PI spectrum observed in the middle of zone 2. At low F_R and F_{PFI}, this assumption appears to be in fair agreement with experimental observation, showing that the peak position obtained by Gaussian fit coincides with the experimentally observed PFI-PI peak position as shown in Figure 5a and Figure 5b. In principle, the PFI-PI peak profile depends on the density of the Rydberg states, and thus, the PFI-PI peak is expected to be asymmetric with its intensity tailing more slowly on the low energy side of the PFI-PI peak. For an ideal F_R and F_{PFI} pulse shape with zero temporal width for the rising and decaying edges, the observed PFI-PI spectrum is expected to exhibit as a rectangular step function. The bottom spectrum of Figure 5b, obtained at F_R = 3.6 V/cm and F_{PFI} = 19.5 V/cm, appears to have a near trapezoidal profile, which can be attributed to the finite rising and decaying slopes of the F_R and F_{PFI} pulses used. As the energy interval of zone 2 decreases for using lower F_R and F_{PFI} values, the trapezoidal profile is expected to merge into a peak-like profile as observed in other PFI-PI spectra of Figure 5a and Figure 5b.

(c) Two-Color Laser PFI-PI Spectra for V$^+$[a^{5}D$_J$ (J = 0−4)], V$^+$[a^{5}F$_J$ (J = 1−5)], and V$^+$[a^{3}F$_J$ (J = 2−4)]. The most important picture coming from this analysis of the Ar$^+$ PFI-PI spectra of Figure 5a and Figure 5b is that the PFI-PI band is bound by the energy region of zone 2, which is determined by the F_R and F_{PFI} pulses applied for the PFI-PI detection. This picture is also confirmed by the observed PFI-PI spectra for the 13 spin−orbit states of the three lowest electronic states V$^+$[a^{5}D$_J$ (J = 0−4)], V$^+$[a^{5}F$_J$ (J = 1−5)], and V$^+$[a^{3}F$_J$ (J = 2−4)] as plotted in Figure 8a, Figure 8b, and Figure 8c, respectively. The IE values for the formation of all these spin−orbit states are known and are marked by long droplines in these figures. We have scanned the UV ω_2 laser beam to cover the energy range needed from below to above the IEs for individual PFI-PI spectra of the V$^+$ spin−orbit states. The pulse field F_R retards prompt ions as well as generate PFI-PIs in zone 1. These PFI-PIs thus generated are retarded along with the prompt ions and so are not included in the PFI-PI spectra. With F_R = 4.0 V/cm, and F_{PFI} = 69.6 V/cm, zone 2 is expected

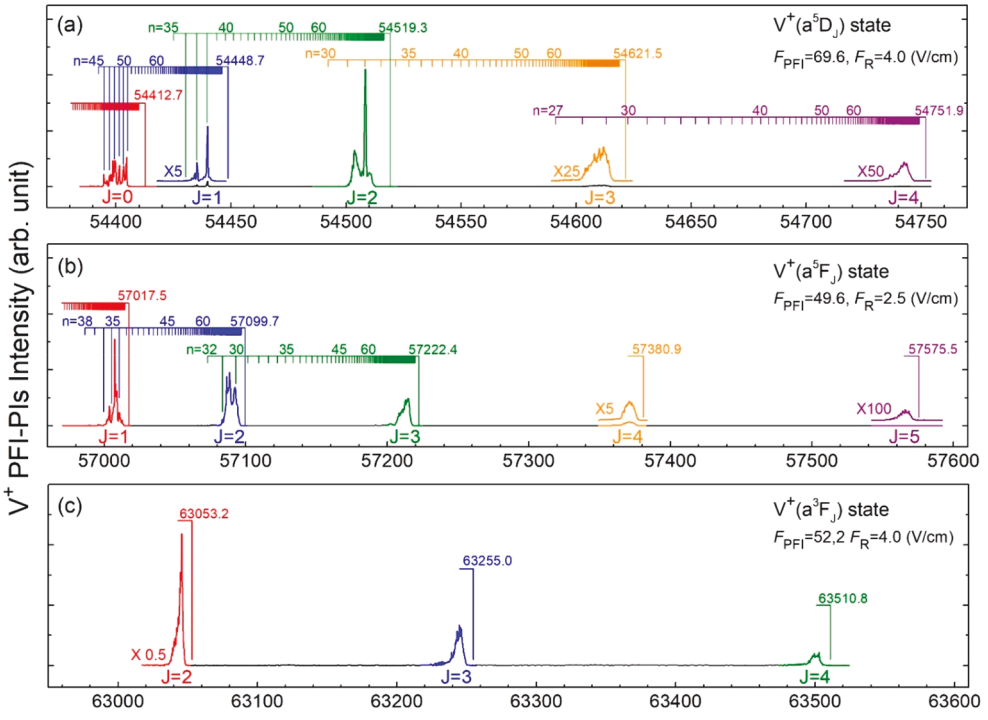

Figure 8. Two-color laser PFI-PI spectra for (a) V$^+$[a^{5}D$_J$ (J = 0−4)], (b) V$^+$[a^{5}F$_J$ (J = 1−5)], and (c) V$^+$[a^{3}F$_J$ (J = 2−4)]. The J state assignments are marked below the PFI-PI spectra for individual spin−orbit electronic states. The F_R and F_{PFI} values used were given in individual figures. The IE values for the formation of all these spin−orbit states are known and are also given and are marked by long dropline shown in these figures. The V$^+$ PFI-PI spectra for V$^+$[a^{5}D$_J$ (J = 0−2)] and V$^+$[a^{5}F$_J$ (J = 1−2)] display well resolved narrow transition structures superimposing on the normal single peak-like PFI-PI spectra observed for V$^+$.

DOI: 10.1021/acs.jpca.9b00511
J. Phys. Chem. A 2019, 123, 2310−2319

to be in the region between 7.7 and 32.0 cm^{-1} below the IE. That is, this V^+ PFI-PI peak has the full-width of about 24 cm^{-1}. The lower limit for the observation of V^+ PFI-PIs is expected to be at ≈32 cm^{-1} below the IE. This prediction based on eq 1 is found to be in excellent accord with the experimental observation, indicating that excited $V^*(n)$ species with $n \geq 60$ can be ionized by the F_{PFI} field pulse.

(d) Identification of Low-*n* Interloper Rydberg States. As shown in Figure 8a, Figure 8b, and Figure 8c, the respective PFI-PI spectra for $V^+[a^5D_J\ (J = 3-4)]$, $V^+[a^5F_J\ (J = 3-5)]$, and $V^+[a^3F_J\ (J = 2-4)]$ are found to exhibit the single peak-like profile similar to that observed in the $Ar^+(^2P_{3/2})$ PFI-PI spectra of Figure 5a and Figure 5b. Several of the V^+ PFI-PI spectra, including those for $V^+[a^5D_J\ (J = 0-2)]$ and $V^+[a^5F_J\ (J = 1-2)]$, display well resolved narrow transition structures superimposed on the normal single peak-like PFI-PI spectra observed for V^+. Many of these narrow transitions are identified as members of the Rydberg series converging to higher spin−orbit states of V^+ as shown below. Limited by the UV ω_2 laser optical bandwidth of 0.15 cm^{-1} (fwhm) used, narrow Rydberg transitions for $n > 80$ cannot be resolved in this study. On the basis of the energy spacing observed between adjacent sharp PFI-PI transitions, they are expected to originate from the Rydberg transition range of $n \approx 40-50$. However, Rydberg states with such low-n values cannot be directly ionized by the Stark fields used. Under the current experimental conditions, the narrow transition structures observed can be attributed to Stark field induced interactions between near resonance high-n Rydberg states and low-n Rydberg interloper states converging to a higher ionization limit. This near-resonance Rydberg state interaction mechanism allows the high-n Rydberg states to borrow intensity from the low-n interloper Rydberg state, resulting in significantly higher PFI-PI intensities observed for the $V^+[a^5D_J\ (J = 0-2)]$ and $V^+[a^5F_J\ (J = 1-2)]$ states.

Equation 2 shows the standard Rydberg series equation, where $E(n)$ is the Rydberg state energy, R is the Rydberg constant 109 736.13 cm^{-1}, and μ is the quantum defect.

$$E(n) = \mathrm{IE} - R/(n-\mu)^2 \quad (2)$$

By use of the $E(n)$ values obtained here and the μ value of 0.88 for the nd Rydberg series determined previously,[38] the least-squares fits to the Rydberg equation yield an IE value for $V^+(a^5D_J)$ of 54 412.65 ± 0.15 cm^{-1}. This value is in excellent agreement with the previous experimentally determined value of 54 413 ± 1 cm^{-1}.[38] James et al. have reported IE(V) = 54 411.67 ± 0.46 cm^{-1} [39] by using resonant two-photon photoionization spectroscopy. Their experiment suffered from Stark shift corrections due to the existence of residual electric field at the PEX region, which could result in larger uncertainties compared to the present measurements. We note that during the laser excitation of V atom in this work, the PEX was maintained field free, and thus, no Stark shift corrections on $E(n)$ are needed. Tables 2 and 3 list the $E(n)$ energies of observed Rydberg peaks superimposing on the $V^+[a^5D_J\ (J = 0)]$ and $V^+[a^5D_J\ (J = 1)]$ PFI-PI spectra, respectively. As shown in the comparisons of Tables 2 and 3 and Figure 8a and Figure 8b, the observed Rydberg PFI-PI peaks are in excellent agreement with their respective predicted members $n = 45-53$ and $n = 36-39$ converging to the $V^+[a^5D_J\ (J = 1)]$ and $V^+[a^5D_J\ (J = 2)]$ states. In the $V^+[a^5D_J\ (J = 2)]$ PFI-PI spectrum, only the very strong peak at 54 508.3 cm^{-1} is identified. On the basis of a similar Rydberg series analysis according to eq 2, we have tentatively assigned this peak to resonance-enhanced interactions with the $n = 32$ Rydberg state converging to the $V^+[a^5D_J\ (J = 3)]$ state. The $V^+[a^5F_J\ (J = 1)]$ and $V^+[a^5F_J\ (J = 2)]$ PFI-PI spectra of Figure 8b also display sharp PFI-PI transition structures. However, the fit of these sharp PFI-PI structures as interloper members of Rydberg series converging to the $V^+[a^5F_J\ (J = 2)]$ and $V^+[a^5F_J\ (J = 3)]$ states is less convincing. Hence, the nature of these sharp transition structures requires further interpretation.

The comparison of the PFI-PI spectra for $V^+[a^5D_J\ (J = 0-4)]$, $V^+[a^5F_J\ (J = 1-5)]$, and $V^+[a^3F_J\ (J = 2-4)]$ in Figure 8a, Figure 8b, Figure 8c, respectively, shows that spectra of low J spin−orbit electronic states are more susceptible to the near-resonance Rydberg interactions, giving rise to more interloper transitions. Since interloper Rydberg states converging to higher J spin−orbit electronic states, which lie at higher energies in the ionization continuum, are expected to have shorter autoionizing lifetimes, the observation of fewer interloper PFI-PI transition structures at PFI-PI spectra of high J states is consistent with this expectation.

Table 2. Comparison of the Experimental Rydberg Energies Observed in the PFI-PI Spectrum for $V^+(a^5D_0)$ with the Least-Squares-Fitted Rydberg Energies of the *n*d Rydberg levels (n = 45−53) Converging to the $V^+(a^5D_1)$ Ion State

Rydberg energy observed in the PFI-PI spectrum for $V^+(a^5D_0)$ (cm^{-1})	least-squares-fitted Rydberg energy converging to $V^+(a^5D_1)$[a] (cm^{-1})	n
54408.10	54408.25	53
54406.77	54406.66	52
54404.82	54404.96	51
54403.08	54403.17	50
54401.22	54401.26	49
54399.26	54399.22	48
54397.09	54397.06	47
54394.70	54394.75	46
54392.21	54392.28	45

[a]Rydberg level energies calculated using the quantum defect $\mu = 0.88$ for the nd Rydberg series converging to $V^+(a^5D_1)$. The least-squares fits to the Rydberg equation yield an IE value of 54412.65 ± 0.15 cm^{-1} for the formation of $V^+[a^5D_J\ (J = 0)]$.

Table 3. Comparison of the Experimental Rydberg Energies Observed in the PFI-PI Spectrum for $V^+(a^5D_2)$ with the Least-Squares-Fitted Rydberg Energies of the *n*d Rydberg levels (n = 36−39) Converging to the $V^+(a^5D_2)$ Ion State

Rydberg energy observed in the PFI-PI spectrum for $V^+(a^5D_1)$ (cm^{-1})	least-squares-fitted Rydberg energy converging to $V^+(a^5D_2)$[a] (cm^{-1})	n
54443.67	54443.76315	39
54439.63	54439.63955	38
54435.38	54435.16874	37
54430.73	54430.31061	36

[a]Rydberg level energies calculated using the quantum defect $\mu = 0.88$ for the nd Rydberg series converging to $V^+(a^5D_2)$. The least-squares fits to the Rydberg equation yield an IE value of 54412.65 ± 0.15 cm^{-1} for the formation of $V^+[a^5D_J\ (J = 0)]$.

IV. CONCLUSIONS

By using a supersonic laser ablation metal beam source to generate a gaseous V atom sample, we have developed a generally applicable quantum state selected V^+ cation beam source with well-defined kinetic energy spreads and sufficiently

DOI: 10.1021/acs.jpca.9b00511
J. Phys. Chem. A 2019, 123, 2310−2319

high intensities for ion−molecule collision dynamics studies. The combination of the two-color laser excitation method and the sequential electric field pulse scheme for PFI-PI detection has made possible the measurements of the fully J resolved PFI-PI spectra for $V^+[a^5D_J\ (J = 0-4)]$, $V^+[a^5F_J\ (J = 1-5)]$, and $V^+[a^3F_J\ (J = 2-4)]$ ions, indicating that the preparation of the V^+ ion in single quantum spin−orbit states can be achieved by employing the experimental scheme presented here. In order to understand the PFI-PI detection mechanism, which is needed to obtain reliable Stark shift corrections, we have also performed detailed VUV PFI-PI measurements of $Ar^+(^2P_{3/2})$ to compare with the two-color PFI-PI spectra of the V^+ ion. This two-color laser PFI-PI scheme can be applied to the quantum spin−orbit selection of other atomic transition metal cations. Thus, the availability of this PFI-PI scheme is expected to allow accurate chemical reactivity measurements of atomic transition metal cations, which are known to play an important role in catalysis and organometallic chemistry.

Due to the consideration of keeping this article in reasonable length, no σ measurements of ion−molecule reactions involving quantum state selected V^+ ion are included here. By using the method described above, we have already obtained detailed chemical reactivity data for the reactions between $V^+(a^5D_J, a^5F_J$, and $a^3F_J)$ and several simple neutral molecules. We plan to publish the results of these reactivity studies in separate forthcoming articles.

AUTHOR INFORMATION

Corresponding Author

*Electronic mail: cyng@ucdavis.edu.

ORCID

Yuntao Xu: 0000-0002-1205-8168

Cheuk-Yiu Ng: 0000-0003-4425-5307

Notes

The authors declare no competing financial interest.

ACKNOWLEDGMENTS

This material is based upon work supported by the National Science Foundation under Grant CHE-1763319. C.-Y.N. is also grateful to Dr. Huie Tarng Liou for his generous donation of research support for the Ng laboratory.

REFERENCES

(1) Armentrout, P. B.; Beauchamp, J. L. The chemistry of atomic transition-metal ions: insight into fundamental aspects of organometallic chemistry. *Acc. Chem. Res.* **1989**, *22* (9), 315−321.

(2) Operti, L.; Rabezzana, R. Gas-phase ion chemistry in organometallic systems. *Mass Spectrom. Rev.* **2006**, *25* (3), 483−513.

(3) Böhme, D. K.; Schwarz, H. Gas-phase catalysis by atomic and cluster metal ions: The ultimate single-site catalysts. *Angew. Chem., Int. Ed.* **2005**, *44* (16), 2336−2354.

(4) Harris, E.; Sinha, B.; van Pinxteren, D.; Tilgner, A.; Fomba, K. W.; Schneider, J.; Roth, A.; Gnauk, T.; Fahlbusch, B.; Mertes, S.; et al. Enhanced role of transition metal ion catalysis during in-cloud oxidation of SO_2. *Science* **2013**, *340* (6133), 727−730.

(5) Irikura, K. K.; Beauchamp, J. Electronic structure considerations for methane activation by third-row transition-metal ions. *J. Phys. Chem.* **1991**, *95* (21), 8344−8351.

(6) Cody, R. B.; Burnier, R. C.; Reents, W. D.; Carlin, T. J.; McCrery, D. A.; Lengel, R. K.; Freiser, B. S. Laser ionization source for ion cyclotron resonance spectroscopy. Application to atomic metal ion chemistry. *Int. J. Mass Spectrom. Ion Phys.* **1980**, *33* (1), 37−43.

(7) Armentrout, P. Electronic state-specific transition metal ion chemistry. *Annu. Rev. Phys. Chem.* **1990**, *41* (1), 313−344.

(8) Simoes, J. M.; Beauchamp, J. Transition metal-hydrogen and metal-carbon bond strengths: the keys to catalysis. *Chem. Rev.* **1990**, *90* (4), 629−688.

(9) Weisshaar, J. C. Control of Transition-Metal Cation Reactivity by Electronic State Selection. In *Advances in Chemical Physics*; Ng, C. Y., Bare, M., Prigogine, I., Rice, S. A., Eds.; John Wiley & Sons, Inc., 1992; DOI: 10.1002/9780470141397.ch3.

(10) Kramida, A.; Ralchenko, Y.; Reader, J.; NIST ASD Team. *NIST Atomic Spectra Database*, version 5.6.1; National Institute of Standards and Technology, 2018;https://doi.org/10.18434/T4W30F.

(11) Condon, E. U.; Condon, E.; Shortley, G. H. *The Theory of Atomic Spectra*; Cambridge University Press, 1951.

(12) Elkind, J.; Armentrout, P. B. Effect of kinetic and electronic energy on the reaction of V^+ with H_2, HD, and D_2. *J. Phys. Chem.* **1985**, *89* (26), 5626−5636.

(13) Koyanagi, G. K.; Bohme, D. K. Gas-phase reactions of carbon dioxide with atomic transition-metal and main-group cations: Room-temperature kinetics and periodicities in reactivity. *J. Phys. Chem. A* **2006**, *110* (4), 1232−1241.

(14) Fisher, E. R.; Elkind, J. L.; Clemmer, D. E.; Georgiadis, R.; Loh, S. K.; Aristov, N.; Sunderlin, L. S.; Armentrout, P. B. Reactions of fourth-period metal ions (Ca^+-Zn^+) with O_2: Metal-oxide ion bond energies. *J. Chem. Phys.* **1990**, *93* (4), 2676−2691.

(15) Aristov, N.; Armentrout, P. B. Methane activation by V^+: electronic and translational energy dependence. *J. Phys. Chem.* **1987**, *91* (24), 6178−6188.

(16) Kickel, B. L.; Armentrout, P. B. Guided ion beam studies of the reactions of Ti^+, V^+, and Cr^+ with silane. Electronic state effects, comparison to reactions with methane, and M^+-SiH_x (x = 0−3) bond energies. *J. Am. Chem. Soc.* **1994**, *116* (23), 10742−10750.

(17) Sanders, L.; Sappey, A. D.; Weisshaar, J. C. Excited state-selected transition metal cations from one-color UV multiphoton ionization. *J. Chem. Phys.* **1986**, *85* (12), 6952−6963.

(18) Sanders, L.; Hanton, S. D.; Weisshaar, J. C. Resonant two photon ionization of V atoms: V+ electronic state distributions and J-resolved photoelectron angular distributions. *J. Chem. Phys.* **1990**, *92* (6), 3485−3497.

(19) Jackson, T. C.; Carlin, T. J.; Freiser, B. S. Gas-phase reactions of V^+ and VO^+ with hydrocarbons using Fourier transform mass spectrometry. *J. Am. Chem. Soc.* **1986**, *108* (6), 1120−1126.

(20) Chang, Y. C.; Xu, H.; Xu, Y.; Lu, Z.; Chiu, Y.-H.; Levandier, D. J.; Ng, C. Y. Communication: Rovibrationally selected study of the $N_2^+(X; v^+=1, N^+=0\text{-}8)$ + Ar charge transfer reaction using the vacuum ultraviolet laser pulsed field ionization-photoion method. *J. Chem. Phys.* **2011**, *134* (20), 201105.

(21) Chang, Y. C.; Xu, Y.; Lu, Z.; Xu, H.; Ng, C. Y. Rovibrationally selected ion-molecule collision study using the molecular beam vacuum ultraviolet laser pulsed field ionization-photoion method: charge transfer reaction of $N_2^+(X^2\Sigma_g^+; v^+=0\text{-}2; N^+=0\text{-}9)$ + Ar. *J. Chem. Phys.* **2012**, *137* (10), 104202.

(22) Xu, Y.; Chang, Y. C.; Lu, Z.; Ng, C. Absolute integral cross sections and product branching ratios for the vibrationally selected ion-molecule reaction:$N_2^+(X^2\Sigma_g^+; v^+=0\text{-}2)+CH_4$. *Astrophys. J.* **2013**, *769* (1), 72.

(23) Xu, Y.; Xiong, B.; Chang, Y. C.; Ng, C. Absolute integral cross sections for the stste-selected ion-molecule reaction $N_2^+(X^2\Sigma_g^+; v^+= 0-2)+ C_2H_2$ in the collision energy range of 0.03−10.00 eV. *Astrophysical Journal* **2016**, *827* (1), 17.

(24) Xu, Y.; Xiong, B.; Chang, Y. C.; Ng, C.-Y. Quantum-state-selected integral cross sections and branching ratios for the ion−molecule reaction of $N_2^+(X^2\Sigma_g^+; v^+=0-2)+C_2H_4$ in the collision energy range of 0.05−10.00 eV. *J. Phys. Chem. A* **2018**, *122* (32), 6491−6499.

(25) Xu, Y.; Xiong, B.; Chang, Y. C.; Ng, C. Y. The translational, rotational, and vibrational energy effects on the chemical reactivity of water cation $H_2O^+(X^2B_1)$ in the collision with deuterium molecule D_2. *J. Chem. Phys.* **2013**, *139* (2), 024203.

(26) Xu, Y.; Xiong, B.; Chang, Y. C.; Ng, C. Y. Communication: Rovibrationally selected absolute total cross sections for the reaction

DOI: 10.1021/acs.jpca.9b00511
J. Phys. Chem. A 2019, 123, 2310−2319

H_2O^+ (X^2B_1; $v_1^+v_2^+v_3^+$ = 000; N^+_{Ka+Kc+}) + D_2: Observation of the rotational enhancement effect. *J. Chem. Phys.* **2012**, *137*, 241101.
(27) Xu, Y.; Xiong, B.; Chang, Y.-C.; Pan, Y.; Lo, P. K.; Lau, K. C.; Ng, C. A quantum-rovibrational-state-selected study of the H_2O^+(X^2B_1:v_1^+,v_2^+,v_3^+; N^+_{Ka+Kb+})+CO reaction in the collision energy range of 0.05−10.00 eV: translational, rotational, and vibrational energy effects. *Phys. Chem. Chem. Phys.* **2017**, *19* (15), 9778−9789.
(28) Xu, Y.; Xiong, B.; Chang, Y. C.; Ng, C.-Y. Quantum-vibrational-state-selected Integral cross sections and product branching ratios for the ion-molecule reactions of N_2^+($X_2\Sigma_g^+$; v^+=0−2)+H_2O and H_2O^+(X^2B_1: $v_1^+v_2^+v_3^+$=000 and 100)+N_2 in the collision energy range of 0.04−10.00 eV. *Astrophysical Journal* **2018**, *861* (1), 17.
(29) Xiong, B.; Chang, Y.-C.; Ng, C.-Y. A quantum-rovibrational-state-selected study of the proton-transfer reaction H_2^+($X^2\Sigma_g^+$:v^+=1-3; N^+=0-3)+Ne→NeH^++H using the pulsed field ionization-photoion method: observation of the rotational effect near the reaction threshold. *Phys. Chem. Chem. Phys.* **2017**, *19* (28), 18619−18627.
(30) Xiong, B.; Chang, Y.-C.; Ng, C.-Y. Quantum-state-selected integral cross sections for the charge transfer collision of O_2^+($a^4\Pi_{u5/2,3/2,1/2,-1/2}$: v^+=1−2; J^+) [O_2^+($X^2\Pi_{g3/2,1/2}$: v^+=22−23; J^+)]+ Ar at center-of-mass collision energies of 0.05−10.00 eV. *Phys. Chem. Chem. Phys.* **2017**, *19* (43), 29057−29067.
(31) Dietz, T. G.; Duncan, M. A.; Powers, D. E.; Smalley, R. E. Laser production of supersonic metal cluster beams. *J. Chem. Phys.* **1981**, *74* (11), 6511−6512.
(32) Reed, B.; Lam, C.-S.; Chang, Y.-C.; Xing, X.; Yang, D.-S.; Ng, C. A high-resolution photoionization study of ^{56}Fe using a vacuum ultraviolet laser. *Astrophys. J.* **2009**, *693* (1), 940.
(33) Chang, Y.-C.; Lam, C.-S.; Reed, B.; Lau, K.-C.; Liou, H.; Ng, C. Rovibronically selected and resolved two-color laser photoionization and photoelectron study of the iron carbide cation. *J. Phys. Chem. A* **2009**, *113* (16), 4242−4248.
(34) Dietrich, H. J.; Lindner, R.; Müller-Dethlefs, K. A new ion detection scheme for ion spectroscopy equivalent to zero kinetic energy photoelectron spectroscopy. *J. Chem. Phys.* **1994**, *101* (4), 3399−3402.
(35) Merkt, F. Molecules in high Rydberg states. *Annu. Rev. Phys. Chem.* **1997**, *48* (1), 675−709.
(36) Seiler, R.; Hollenstein, U.; Greetham, G. M.; Merkt, F. Rydberg-state-resolved zero-kinetic-energy photoelectron spectroscopy. *Chem. Phys. Lett.* **2001**, *346* (3−4), 201−208.
(37) *PeakFIT*, version 4.11; Systat Software Inc.; http://www.sigmaplot.co.uk/downloads/download.php#peak.
(38) Page, R. H.; Gudeman, C. S. Completing the iron period: double-resonance, fluorescence-dip Rydberg spectroscopy and ionization potentials of titanium, vanadium, iron, cobalt, and nickel. *J. Opt. Soc. Am. B* **1990**, *7* (9), 1761−1771.
(39) James, A. M.; Kowalczyk, P.; Langlois, E.; Campbell, M. D.; Ogawa, A.; Simard, B. Resonant two photon ionization spectroscopy of the molecules V2, VNb, and Nb2. *J. Chem. Phys.* **1994**, *101* (6), 4485−4495.

DOI: 10.1021/acs.jpca.9b00511
J. Phys. Chem. A 2019, 123, 2310−2319